

Lawrence Berkeley National Laboratory

LBL Publications

Title

Cation- and lattice-site-selective magnetic depth profiles of ultrathin Fe₃O₄(001) films

Permalink

<https://escholarship.org/uc/item/5k449911>

Journal

Physical Review B, 102(22)

ISSN

2469-9950

Authors

Pohlmann, Tobias
Kuschel, Timo
Rodewald, Jari
[et al.](#)

Publication Date





2020-12-01

DOI

10.1103/physrevb.102.220411

Peer reviewed

Cation- and lattice-site-selective magnetic depth profiles of ultrathin Fe₃O₄(001) films

Tobias Pohlmann ^{1,2,*} Timo Kuschel ³ Jari Rodewald,¹ Jannis Thien,¹ Kevin Ruwisch,¹ Florian Bertram,² Eugen Weschke,⁴ Padraic Shafer,⁵ Joachim Wollschläger ^{1,†} and Karsten Küpper ^{1,‡}

¹Department of Physics, Osnabrück University, Barbarastr. 7, 49076 Osnabrück, Germany

²DESY Photon Science, Notkestr. 85, 22607 Hamburg, Germany

³Center for Spinelectronic Materials and Devices, Department of Physics, Bielefeld University, Universitätsstr. 25, 33615 Bielefeld, Germany

⁴Helmholtz-Zentrum Berlin für Materialien und Energie, Wilhelm-Conrad-Röntgen-Campus BESSY II, Albert-Einstein-Strasse 15, 12489 Berlin, Germany

⁵Advanced Light Source, Lawrence Berkeley National Laboratory, 6 Cyclotron Rd., Berkeley, California 94720, USA

A detailed understanding of ultrathin film surface properties is crucial for the proper interpretation of spectroscopic, catalytic, and spin-transport data. We present x-ray magnetic circular dichroism (XMCD) and x-ray resonant magnetic reflectivity (XRMR) measurements on ultrathin Fe₃O₄ films to obtain magnetic depth profiles for the three resonant energies corresponding to the different cation species Fe_{oct}²⁺, Fe_{tet}³⁺, and Fe_{oct}³⁺ located on octahedral and tetrahedral sites of the inverse spinel structure of Fe₃O₄. By analyzing the XMCD spectrum of Fe₃O₄ using multiplet calculations, the resonance energy of each cation species can be isolated. Performing XRMR on these three resonant energies yields magnetic depth profiles that each correspond to one specific cation species. The depth profiles of both kinds of Fe³⁺ cations reveal a (3.9 ± 1.0)-Å-thick surface layer of enhanced magnetization, which is likely due to an excess of these ions at the expense of the Fe_{oct}²⁺ species in the surface region. The magnetically enhanced Fe_{tet}³⁺ layer is additionally shifted about 2.9 ± 0.4 Å farther from the surface than the Fe_{oct}³⁺ layer.

I. INTRODUCTION

Magnetite, Fe₃O₄, is one of the most frequently investigated transition-metal oxides, since it is a key material in spintronics [1], spin caloritronics [2], and material chemistry [3]. Fe₃O₄ thin films were considered highly suitable as electrode material for magnetic tunnel junctions [4,5] due to their predicted half-metallic behavior with 100% spin polarization [6]. However, the promise was never quite met, with modest tunnel magnetoresistance ratios ranging from -26% to 18% [4,5,7]. In order to test its half-metallicity, spin-resolved x-ray photoelectron spectroscopy (SR-XPS) on Fe₃O₄(111) films found a spin polarization of about 80% [8], while on Fe₃O₄(001) the same technique yielded polarizations of 40%–70% [9–11].

Both the reduced tunnel magnetoresistance and the deviations from 100% spin polarization in SR-XPS were argued to emerge from interface and surface effects, respectively [4,5,8,10,11]. For Fe₃O₄(111) films deposited on semiconducting ZnO(0001), lattice-site-selective depth profiles obtained by x-ray resonant magnetic reflectivity (XRMR) and electron energy loss spectroscopy did not find a notable surface modification apart from a Fe_{oct} termination [12]. Reduction of the spin polarization measured at the Fe₃O₄(001)

surface was typically considered to originate from a surface reconstruction, the existence of which has long been known but only recently has been resolved as a subsurface cation vacancy (SCV) structure [13]. This revelation highlights the issues that might arise from generalizing results from surface-sensitive techniques, such as x-ray absorption spectroscopy (XAS) in total electron yield (TEY) mode and x-ray photoelectron spectroscopy (XPS), to explain the behavior of the bulk material [14].

In particular, drawing conclusions about the cation distribution of magnetite requires caution, because the bulk material of the inverse spinel Fe₃O₄ should contain divalent Fe_{oct}²⁺, as well as trivalent ions in both octahedral and tetrahedral coordination, Fe_{tet}³⁺ and Fe_{oct}³⁺. In contrast, the DFT+*U* calculations of the SCV structure predict the first four atomic layers to only contain Fe³⁺ ions and to have a formal stoichiometry of Fe₁₁O₁₆, in agreement with earlier reports on an excess of Fe³⁺ at the (001) surface [15]. But while the SCV model has been very successful in explaining low-energy electron diffraction (LEED) and adsorption data [13,16], a spatial depth resolution has yet to be achieved. It also remains unclear what happens to the Fe₃O₄(001) surface when it is exposed to air and loses the (√2 × √2)R45° LEED pattern characteristic for the SCV structure.

In this Rapid Communication, we report an investigation of the magnetic surface properties of ultrathin Fe₃O₄(001) films, in contrast to the bulk, by recording magneto-optical depth profiles of the three cation species in Fe₃O₄. The L_{2,3} x-ray magnetic circular dichroism (XMCD) spectrum of

*tobias.pohlmann@desy.de

†jwollsch@uni-osnabrueck.de

‡kkuepper@uni-osnabrueck.de

magnetite exhibits three extrema at energies characteristic for the $\text{Fe}_{\text{oct}}^{2+}$, $\text{Fe}_{\text{tet}}^{3+}$, and $\text{Fe}_{\text{oct}}^{3+}$ cations. We employ XRMR at those characteristic energies to determine the magneto-optical depth profiles of ultrathin $\text{Fe}_3\text{O}_4/\text{MgO}(001)$ films for each individual cation species. We find an ≈ 3.9 Å layer of enhanced magneto-optical absorption at the surface at the resonant energies of both Fe^{3+} species but not for Fe^{2+} , suggesting an Fe^{3+} -rich surface.

II. EXPERIMENTAL AND THEORETICAL DETAILS

We prepared a 25-nm Fe_3O_4 film on $\text{MgO}(001)$ in a multichamber ultrahigh-vacuum system using reactive molecular beam epitaxy (RMBE). Iron was deposited in an oxygen atmosphere of 5×10^{-6} mbar onto $\text{MgO}(001)$ at 250 °C. Its chemical composition and $(\sqrt{2} \times \sqrt{2})R45^\circ$ superstructure was confirmed by *in situ* XPS and LEED, respectively. For details on the deposition and characterization methods, please see Refs. [17,18]. Additionally, two other films of 13 and 50 nm Fe_3O_4 were deposited on $\text{MgO}(001)$. The complementary results obtained from these films are presented in the Supplemental Material [19] (Sec. A).

For the XAS and XMCD study, the sample was transferred from our laboratory under ambient conditions to the Superconducting Vector Magnet Endstation at beamline 4.0.2 of the Advanced Light Source (ALS). It was measured at room temperature in a magnetic field of 4 T along the x-ray beam. The incidence angle of the x-rays was 30° from the [100] direction of Fe_3O_4 , and the degree of circular polarization was 90%. The XAS and XMCD spectra were measured across the Fe $L_{2,3}$ absorption edges (690–750 eV). All XAS spectra were measured in the TEY mode, which has a probing depth in magnetite of about 3 nm [20].

The XAS and XMCD data were analyzed by applying the sum rules [21–23] and charge-transfer multiplet calculations using the Thole code [24] with the assistance of CTM4XAS [25,26]. For the sum rules, we took into account a correction factor of 1.142 derived by Teramura *et al.* for Fe^{2+} [23] and assumed $14 \frac{\text{holes}}{\text{f.u.}}$. For the multiplet calculations, we assumed the three-cation model, using crystal field and charge-transfer parameters as described in Ref. [17]. The parameters and more details regarding the multiplet calculations can also be found in the Supplemental Material [19] (Sec. B, including Refs. [27,28]). The multiplet states resulting from these calculations were compared to the data by assuming a Gaussian instrumental broadening of 0.2 eV, and a Lorentzian lifetime broadening of 0.3 eV at L_3 and 0.6 eV at L_2 .

The sample was transferred to BESSY II under ambient conditions and x-ray reflectivity (XRR) and XRMR were performed in the XUV diffractometer at beamline UE46_PGM-1 [29]. It was placed between two permanent magnets in a magnetic field of 200 mT longitudinal in regard to the x-ray beam, at room temperature. The x-rays had a degree of circular polarization of 90%. First, we characterized the structural properties (thickness d , roughness σ) by XRR at off-resonant energies (680 eV, 1000 eV). Second, XAS and XMCD were measured in order to select suitable energies for XRMR. Finally, θ - 2θ scans in the range $2\theta = 0^\circ$ – 140° at resonant energies E_i with extrema in the XMCD signal [maximum at 708.4 eV, minimum at 709.5 eV, maximum

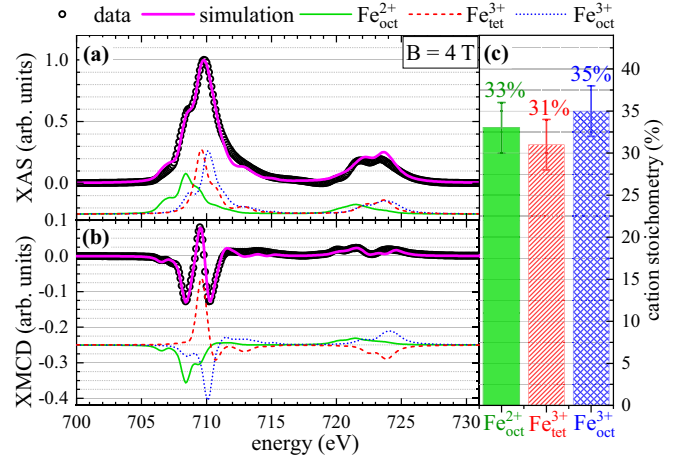


FIG. 1. (a) XAS and (b) XMCD spectrum at the Fe $L_{2,3}$ edge for the Fe_3O_4 film, taken at 4 T external magnetic field, at room temperature, and in TEY mode. A step function was subtracted from the XAS spectrum. Black dots represent data; green, red, and blue spectra are multiplet calculations for the three cation species of Fe_3O_4 , and the violet line is their sum. The cation spectra are offset for better visibility. (c) Cation stoichiometry used to obtain the fit in (a) and (b).

at 710.2 eV, cf. Fig. 1(b)] were performed with both right and left circularly polarized x-rays, to obtain the averaged resonant “nondichroic” XRR curve, $I = (I^{\text{right}} + I^{\text{left}})/2$, and the XRMR asymmetry ratios

$$\Delta I = \frac{I^{\text{right}} - I^{\text{left}}}{I^{\text{right}} + I^{\text{left}}}. \quad (1)$$

These curves were then fitted with the Zak matrix formalism using the software REMAGX to determine the depth profiles of the complex refractive index $n(z)$ [30]. Assuming an in-plane magnetization longitudinal to the x-ray beam, it can be written as

$$n(z) = 1 - \delta(z) + i\beta(z) \pm [\Delta\delta(z) - i\Delta\beta(z)]\cos(\theta), \quad (2)$$

with the magneto-optical absorption $\Delta\beta(z)$ and dispersion $\Delta\delta(z)$ along the film height z . The optical absorption β is proportional to the XAS signal, while the magneto-optical absorption $\Delta\beta$ is proportional to the XMCD signal [30]. Thus, $\Delta\beta(z)$ is a measure of the magnetization along the film depth. $\delta(E)$ and $\beta(E)$, as well as $\Delta\delta(E)$ and $\Delta\beta(E)$, are coupled by the Kramers-Kronig relations, which for symmetric extrema dictate $\Delta\delta(E_0) = 0$ if $\Delta\beta(E)$ has a maximum at E_0 [31]. For this reason, we set $\Delta\delta(z) = 0$ for all models [32]. A detailed review of the XRMR method and the software is given in Ref. [30], and conclusive recipes for fitting XRMR data can be found in Refs. [33–35].

III. RESULTS

The model to fit the off-resonant XRR data consists of a Fe_3O_4 film of 25.2 ± 0.3 nm thickness and an interface roughness $\sigma^{\text{int}} = 3.5 \pm 0.5$ Å and a surface roughness of $\sigma^{\text{surf}} = 3.3 \pm 0.5$ Å. An optically thin surface layer of 12 Å had to be included, likely stemming from adatoms settling on the surface upon the exposure to air. However, this layer does

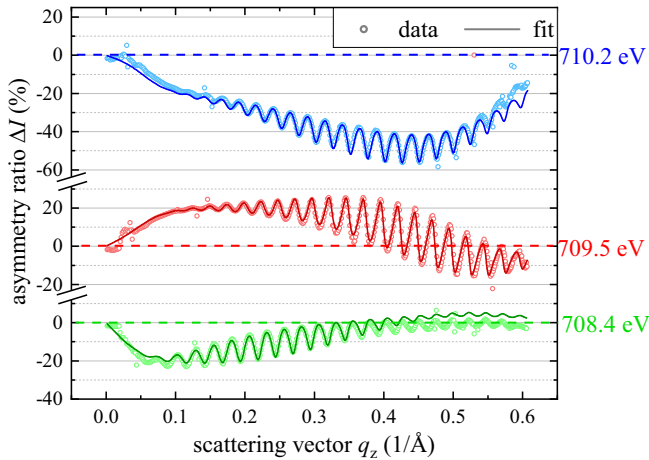


FIG. 2. XRMR data (open circles) and corresponding fits (solid lines) from the Fe_3O_4 film, recorded at the three resonant energies of the XMCD L_3 edge, using the modeled magneto-optical depth profiles of Fig. 3(a). Data were recorded with a magnetic field of 200 mT along the $\text{Fe}_3\text{O}_4[001]$ direction at room temperature.

not contribute to the magnetic signal. The resulting density profile can be seen as a black line in Fig. 3(a). The XRR curves of the 25-nm sample can be found in the Supplemental Material [19] (Sec. C).

Figure 1 shows the XAS and XMCD spectra of the Fe_3O_4 film, recorded at ALS. Corresponding data measured at BESSY II, under the same conditions in which the XRMR was

TABLE I. Contributions of the three cation species to the extrema in the XMCD spectrum in Fig. 1(b), as obtained by the multiplet analysis using Eq. (3).

Energy	$\text{Fe}_{\text{oct}}^{2+}$	$\text{Fe}_{\text{tet}}^{3+}$	$\text{Fe}_{\text{oct}}^{3+}$
708.4 eV	$73 \pm 5\%$	$-8 \pm 3\%$	$19 \pm 5\%$
709.5 eV	$18 \pm 3\%$	$-64 \pm 3\%$	$18 \pm 3\%$
710.2 eV	$4 \pm 3\%$	$-16 \pm 8\%$	$80 \pm 10\%$

performed, can be found in the Supplemental Material [19] (Sec. B). The spin and orbital moments obtained from the sum rules are $\mu_{\text{spin}} = 3.5 \pm 0.3\mu_{\text{B}}/\text{f.u.}$ and $\mu_{\text{orb}} = 0.09 \pm 0.02\mu_{\text{B}}/\text{f.u.}$ Their sum is slightly reduced compared to the bulk value of magnetite of $\mu = \mu_{\text{spin}} + \mu_{\text{orb}} = 4.07\mu_{\text{B}}$ [36]. This behavior of magnetite films has been observed previously [17], and can be explained by a higher density of antiphase boundaries (APBs) for thin films due to the antiferromagnetic coupling across APBs reducing the average magnetic moment of the film [37–39]. Additionally, multiplet simulations are fitted to the XMCD data [cf. Fig. 1(b)]. By weighting the individual spectra with respect to the cation stoichiometry given in Fig. 1(c), the XAS and XMCD data can be described well by our model (cf. violet lines). Thus, the cation distribution on different sites almost follows the ideal stoichiometry of 1:1:1, with a slight excess of $\text{Fe}_{\text{oct}}^{3+}$.

One feature of this kind of modeling is the fact that each of the three extrema observed in the XMCD spectrum can mainly be attributed to one cation spectrum. Table I shows the contributions $r^{\text{cation}}(E_i)$ of each cation spectrum at the resonant energies E_i in the XMCD spectrum, according to

$$r^{\text{cation}}(E_i) = \frac{I^{\text{cation}}(E_i)}{|I^{\text{Fe}_{\text{oct}}^{2+}}(E_i)| + |I^{\text{Fe}_{\text{tet}}^{3+}}(E_i)| + |I^{\text{Fe}_{\text{oct}}^{3+}}(E_i)|}, \quad (3)$$

with $I^{\text{cation}}(E_i)$ being the XMCD signal of the corresponding cation spectrum in Fig. 1(b) at energies $E_i = 708.4, 709.5, 710.2$ eV. While there still is a considerable mixing, at least 64% of each extremum can be attributed to its dominant cation.

Accordingly, the strategy to obtain cationic depth profiles is to pick the three corresponding XMCD resonant energies and perform XRMR measurements at these resonances. Figure 2 shows the asymmetry ratios ΔI and their fits at the three XMCD resonant energies for the Fe_3O_4 film. The near-surface region of the magneto-optical depth profiles $\Delta\beta(z)$ that generate the fits are shown in Fig. 3(a), together with the density depth profile obtained from off-resonant XRR (black line). The most striking feature is the behavior at the surface: at the $\text{Fe}_{\text{oct}}^{2+}$ resonance energy (708.4 eV, green), the magneto-optical depth profile in fact appears to just follow the density profile. However, at both the $\text{Fe}_{\text{tet}}^{3+}$ and the $\text{Fe}_{\text{oct}}^{3+}$ resonance energies, there are noticeable changes to the $\Delta\beta$ depth profiles. In order to fit their asymmetry ratios, we must include a thin surface layer of enhanced magneto-optical absorption. The obvious choice of magneto-optical depth profiles which are simply homogeneous through the entire film did not provide satisfactory fits to the data. This necessity is discussed in more detail in the Supplemental Material [19] (Sec. C). The edge of the magneto-optical depth profile of the $\text{Fe}_{\text{oct}}^{2+}$ resonance

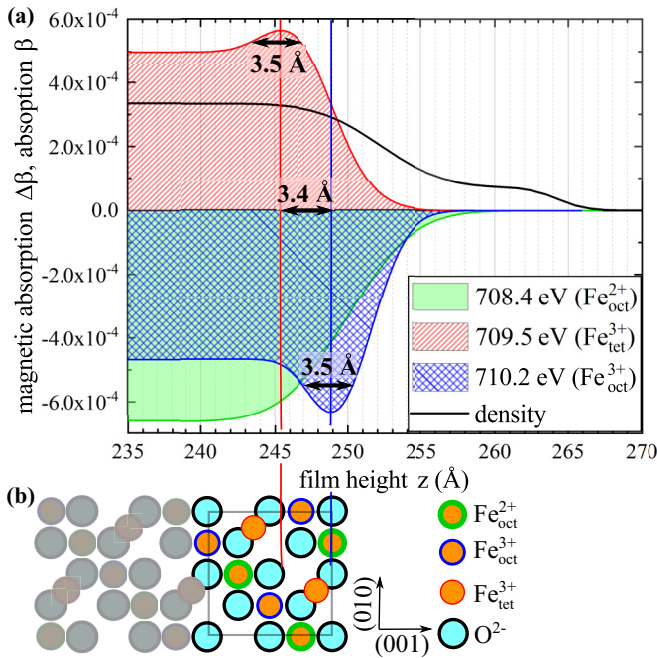


FIG. 3. (a) Close-up of the surface magneto-optical depth profile of the Fe_3O_4 film, together with the optical density obtained from off-resonant XRR fits (black line). (b) $(\text{Fe}_{\text{oct}}\text{-O})$ -terminated model of the magnetite unit cell, in scale with Fig. 3(a). Comparison with the model in (b) illustrates the sizes of the enhanced regions being roughly half a unit cell of magnetite (four cation layers).

roughly matches the location of the magnetically enhanced $\text{Fe}_{\text{tet}}^{3+}$ layer. The thickness of the magnetically enhanced layers is about $d^{\text{enh}} = 3.5 \text{ \AA}$ for both Fe^{3+} species. This corresponds to slightly less than half a bulk unit cell of magnetite ($a/2 = 4.2 \text{ \AA}$), as illustrated by Fig. 3(b). Furthermore, the magnetically enhanced layers are not colocated at the same depth: the magnetically enhanced $\text{Fe}_{\text{tet}}^{3+}$ layer is shifted about $\Delta z^{\text{enh}} = 3.4 \text{ \AA}$ deeper into the film than the magnetically enhanced $\text{Fe}_{\text{oct}}^{3+}$ layer. We performed the same experiment on two other samples of different thicknesses, 13 and 50 nm. The above results are robust among these three samples with some variation in the values for d^{enh} and Δz^{enh} . From this variation, we estimate $d^{\text{enh}} = 3.9 \pm 1.0 \text{ \AA}$ and $\Delta z^{\text{enh}} = 2.9 \pm 0.4 \text{ \AA}$. More details on the results of the two other samples can be found in the Supplemental Material [19] (Sec. A).

IV. DISCUSSION

The magneto-optical depth profiles are not identical with the depth distribution of the cations: As quantified in Table I, the signal on each resonance is a mixture of contributions from all three cations. For the magneto-optical depth profile at 710.2 eV approximately 80% of the signal originates from the $\text{Fe}_{\text{oct}}^{3+}$ and is therefore strongly dominated by this species. And since the position of the layer of enhanced magnetization at 709.5 eV does not match the position of the 710.2 eV layer, we can conclude it to be a distinct physical feature, stemming from the $\text{Fe}_{\text{tet}}^{3+}$ species.

There are two possible explanations for the enhanced magnetization layer: either the magnetic scattering factors of the Fe^{3+} cations at the surface are enhanced, or the surface stoichiometry is changed. However, an increase in the magnetic scattering factor large enough to explain the observation would require an increase of the magnetic moment of the individual cations, which in Fe_3O_4 are already in the high-spin state with $5\mu_B$. This explanation is therefore implausible.

One ansatz is to take into account rearranged cation distributions due to the reconstructed $\text{Fe}_3\text{O}_4(001)$ surface as proposed by the SCV model [13,14], although in our films no reconstruction is visible in LEED anymore when the XRMR measurements are performed. The SCV model predicts that, in order to achieve polarity compensation, the first unit cell contains only Fe^{3+} species, with the first $\text{Fe}_{\text{tet}}^{3+}$ layer lying about 1 \AA deeper than the $\text{Fe}_{\text{oct}}^{3+}$. This model matches surprisingly well some aspects of our findings. The first $\text{Fe}_{\text{oct}}\text{-O}$ layer remains stoichiometric, but the $\text{Fe}_{\text{oct}}^{2+}$ changes valency to $\text{Fe}_{\text{oct}}^{3+}$, effectively doubling the $\text{Fe}_{\text{oct}}^{3+}$ density. In the second layer, an additional $\text{Fe}_{\text{tet}}^{3+}$ ion is added, increasing the $\text{Fe}_{\text{tet}}^{3+}$ density by 50%. However, we do not observe the depletion of $\text{Fe}_{\text{oct}}^{2+}$ cations in the first 8.4 \AA and the enhancements of $\text{Fe}_{\text{tet}}^{3+}$ and $\text{Fe}_{\text{oct}}^{3+}$ are less than expected from the SCV model. Also, the $\text{Fe}_{\text{oct}}^{2+}$ cations still exist in the surface layer to some amount while the SCV model predicts their complete conversion to $\text{Fe}_{\text{oct}}^{3+}$. This agreement is surprising because it is known that Fe_3O_4 surfaces hydroxylate on ambient conditions and do not show the $(\sqrt{2} \times \sqrt{2})R45^\circ$ LEED pattern, but instead a (1×1) pattern [14]. This may be attributed to disorder at the surface with loss of long-range order while the local order of vacancies and interstitials is kept. Since our samples were exposed to air before the XRMR measurements, they are in

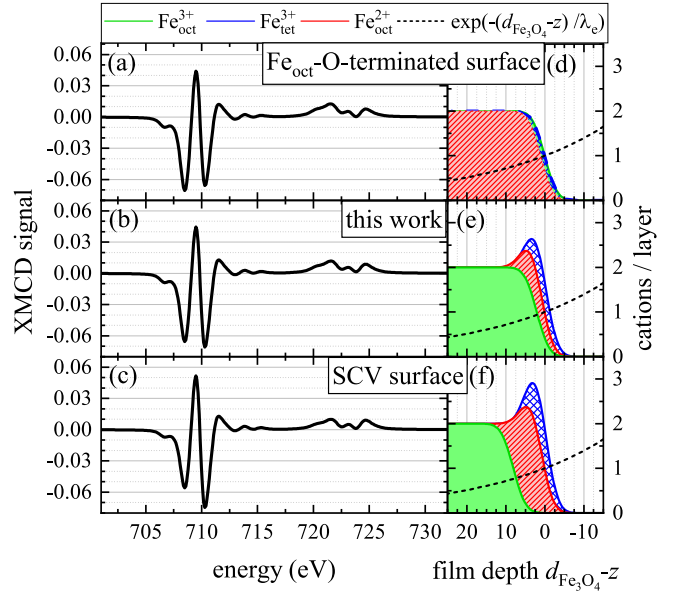


FIG. 4. Multiplet simulations of XMCD spectra collected in TEY mode expected for (a) a $\text{Fe}_{\text{oct}}\text{-O}$ -terminated $\text{Fe}_3\text{O}_4(001)$ surface, (b) the surface found in this work, and (c) an ideal SCV surface. (d)–(f) Cation profiles for each model, with a simulated roughness of 2.5 \AA . The dashed line indicates the sensitivity of the TEY signal on the sample depth $d_{\text{Fe}_3\text{O}_4} - z$, which exponentially decays with the electron escape depth $\lambda_e = 30 \text{ \AA}$.

this seemingly unreconstructed state, but the magneto-optical depth profiles are consistent with an intermediate stoichiometry between bulk termination and the SCV surface. Our results now suggest that even in that case, at least the Fe^{3+} enrichment of the surface remains intact. A more detailed comparison of the SCV model to our findings can be found in the Supplemental Material [19] (Sec. D).

An excess of Fe^{3+} cations on the surface can warp the interpretation of surface-sensitive techniques. Figure 4 shows multiplet simulations of the XMCD spectra collected in TEY mode of (a) the $\text{Fe}_{\text{oct}}\text{-O}$ -terminated surface, (b) the surface stoichiometry found in this work, and (c) the SCV surface. For the simulations, the individual cation spectra were calculated using the multiplet parameters from Fig. 1, and weighted by the corresponding model cation profiles shown in Figs. 4(d)–4(f), for which we used a simulated surface roughness of 2.5 \AA . The surface sensitivity of TEY was modeled by an exponential decay of the signal with the electron escape depth $\lambda_e = 30 \text{ \AA}$, indicated by the dashed black lines in Figs. 4(d)–4(f). The modeled XMCD spectra mostly differ in the amplitudes of the 708.4 and 710.2 eV features, which are most sensitive to the $\text{Fe}_{\text{oct}}^{2+}$ and $\text{Fe}_{\text{oct}}^{3+}$ species, respectively. This can cause an overestimation of the $\text{Fe}_{\text{oct}}^{3+}$ species, if TEY data from the $\text{Fe}_3\text{O}_4(001)$ surface are applied as a measure of the bulk material, as is evident in Fig. 1(c). Similar results can be expected for other surface-sensitive techniques, such as XPS, and have to be taken into account in the interpretation of the data, depending on the necessary accuracy of the evaluation. Particularly, the antiferromagnetic coupling between $\text{Fe}_{\text{oct}}^{3+}$ and $\text{Fe}_{\text{tet}}^{3+}$ remains intact, which implies a reduction of the spin polarization on the surface, consistent with the low spin po-

larization found in SR-XPS on $\text{Fe}_3\text{O}_4(001)$ surfaces [9–11]. A comparison of Figs. 4(b) and 4(c) reveals that for samples exposed to air, this effect is weakened compared to what is expected for a pure SCV surface.

V. SUMMARY

In conclusion, we fabricated a $\text{Fe}_3\text{O}_4/\text{MgO}(001)$ ultra-thin film by RMBE. We recorded XAS/XMCD at ALS beamline 4.0.2 as well as XAS/XMCD and XRMR measurements at BESSY II beamline UE46_PGM-1, in order to obtain magneto-optical depth profiles. By fitting multiplet calculations to the XMCD data, we determine the cation contributions at the three resonant energies of the XMCD spectrum, and use XRMR at those energies in order to resolve the magneto-optical depth profiles of the three iron species in Fe_3O_4 . We find that both Fe^{3+} species show an enhanced signal in the near-surface region in an $\approx(3.9 \pm 1.0)$ -Å-thick layer, with the $\text{Fe}_{\text{tet}}^{3+}$ layer located about 2.9 ± 0.4 Å under-

neath the $\text{Fe}_{\text{oct}}^{3+}$ layer. We attribute this to the first unit cell from the surface containing an excess of Fe^{3+} cations. This result needs to be considered in the interpretation of surface-sensitive spectroscopic techniques.

ACKNOWLEDGMENTS

Financial support from the Bundesministerium für Bildung und Forschung (FKZ 05K16MP1) is gratefully acknowledged. We are also grateful for the kind support from the Deutsche Forschungsgemeinschaft (DFG under Grants No. KU2321/6-1 and No. WO533/20-1). This research used resources of the Advanced Light Source, a DOE Office of Science User Facility under Contract No. DE-AC02-05CH11231, by recording XMCD at beamline 4.0.2 (ALS-10261). We thank HZB for the allocation of synchrotron beamtime at beamline UE46_PGM-1 (181/06266ST/R) where we recorded the XRMR and additional XMCD measurements.

- [1] J.-B. Moussy, *J. Phys. D* **46**, 143001 (2013).
- [2] R. Ramos, T. Kikkawa, K. Uchida, H. Adachi, I. Lucas, M. H. Aguirre, P. Algarabel, L. Morellón, S. Maekawa, E. Saitoh, and M. R. Ibarra, *Appl. Phys. Lett.* **102**, 072413 (2013).
- [3] M. Lin and H. Leu, *Electroanalysis* **17**, 2068 (2005).
- [4] T. Kado, *Appl. Phys. Lett.* **92**, 092502 (2008).
- [5] L. Marnitz, K. Rott, S. Niehörster, C. Klewe, D. Meier, S. Fabretti, M. Witzkiok, A. Krampf, O. Kuschel, T. Schemme, K. Kuepper, J. Wollschläger, A. Thomas, G. Reiss, and T. Kuschel, *AIP Adv.* **5**, 047103 (2015).
- [6] Z. Zhang and S. Satpathy, *Phys. Rev. B* **44**, 13319 (1991).
- [7] G. Hu and Y. Suzuki, *Phys. Rev. Lett.* **89**, 276601 (2002).
- [8] Y. S. Dedkov, U. Rüdiger, and G. Güntherodt, *Phys. Rev. B* **65**, 064417 (2002).
- [9] J. G. Tobin, S. A. Morton, S. W. Yu, G. D. Waddill, I. K. Schuller, and S. A. Chambers, *J. Phys.: Condens. Matter* **19**, 315218 (2007).
- [10] M. Fonin, Y. S. Dedkov, R. Pentcheva, U. Rüdiger, and G. Güntherodt, *J. Phys.: Condens. Matter* **20**, 142201 (2008).
- [11] W. Wang, J.-M. Mariot, M. C. Richter, O. Heckmann, W. Ndiaye, P. De Padova, A. Taleb-Ibrahimi, P. Le Fèvre, F. Bertran, F. Bondino, E. Magnano, J. Krempaský, P. Blaha, C. Cacho, F. Parmigiani, and K. Hricovini, *Phys. Rev. B* **87**, 085118 (2013).
- [12] S. Brück, M. Paul, H. Tian, A. Müller, D. Kufer, C. Praetorius, K. Fauth, P. Audehm, E. Goering, J. Verbeeck, G. Van Tendeloo, M. Sing, and R. Claessen, *Appl. Phys. Lett.* **100**, 081603 (2012).
- [13] R. Bliem, E. McDermott, P. Ferstl, M. Setvin, O. Gamba, J. Pavelec, M. A. Schneider, M. Schmid, U. Diebold, P. Blaha, L. Hammer, and G. S. Parkinson, *Science* **346**, 1215 (2014).
- [14] G. S. Parkinson, *Surf. Sci. Rep.* **71**, 272 (2016).
- [15] S. Chambers and S. Joyce, *Surf. Sci.* **420**, 111 (1999).
- [16] R. Bliem, J. Pavelec, O. Gamba, E. McDermott, Z. Wang, S. Gerhold, M. Wagner, J. Osiecki, K. Schulte, M. Schmid, P. Blaha, U. Diebold, and G. S. Parkinson, *Phys. Rev. B* **92**, 075440 (2015).
- [17] K. Kuepper, O. Kuschel, N. Pathé, T. Schemme, J. Schmalhorst, A. Thomas, E. Arenholz, M. Gorgoi, R. Ovsyannikov, S. Bartkowski, G. Reiss, and J. Wollschläger, *Phys. Rev. B* **94**, 024401 (2016).
- [18] O. Kuschel, R. Buß, W. Spiess, T. Schemme, J. Wöllermann, K. Balinski, A. T. N’Diaye, T. Kuschel, J. Wollschläger, and K. Kuepper, *Phys. Rev. B* **94**, 094423 (2016).
- [19] See Supplemental Material at <http://link.aps.org/supplemental/10.1103/PhysRevB.102.220411> for XMCD, XRR, and XRMR data for two $\text{Fe}_3\text{O}_4/\text{MgO}$ films of different thicknesses which show the same behavior, and for details on the multiplet calculations. It also further illustrates the necessity to include the layers of enhanced magnetization in order to properly fit the XRMR data, and contains a thorough comparison of our model to the SCV model.
- [20] G. F. M. Gomes, T. E. P. Bueno, D. E. Parreiras, G. J. P. Abreu, A. de Siervo, J. C. Cezar, H.-D. Pfannes, and R. Paniago, *Phys. Rev. B* **90**, 134422 (2014).
- [21] C. Piamonteze, P. Miedema, and F. M. F. de Groot, *Phys. Rev. B* **80**, 184410 (2009).
- [22] C. T. Chen, Y. U. Idzerda, H.-J. Lin, N. V. Smith, G. Meigs, E. Chaban, G. H. Ho, E. Pellegrin, and F. Sette, *Phys. Rev. Lett.* **75**, 152 (1995).
- [23] Y. Teramura, A. Tanaka, and T. Jo, *J. Phys. Soc. Jpn.* **65**, 1053 (1996).
- [24] G. van der Laan, *J. Electron Spectrosc. Relat. Phenom.* **86**, 41 (1997).
- [25] F. de Groot, *Coord. Chem. Rev.* **249**, 31 (2005).
- [26] E. Stavitski and F. M. de Groot, *Micron* **41**, 687 (2010).
- [27] T. J. Regan, H. Ohldag, C. Stamm, F. Nolting, J. Lüning, J. Stöhr, and R. L. White, *Phys. Rev. B* **64**, 214422 (2001).
- [28] C. T. Chantler, *J. Phys. Chem Ref. Data* **24**, 71 (1995).
- [29] E. Weschke and E. Schierle, *Journal of Large-Scale Research Facilities* **4**, A127 (2018).
- [30] S. Macke and E. Goering, *J. Phys.: Condens. Matter* **26**, 363201 (2014).
- [31] J. Als-Nielsen and D. McMorrow, *Elements of Modern X-ray Physics* (Wiley, New York, 2011).
- [32] P. Bougiatioti, O. Manos, O. Kuschel, J. Wollschläger, M. Tolkieln, S. Francoual, and T. Kuschel, [arXiv:1807.09032](https://arxiv.org/abs/1807.09032).

- [33] T. Kuschel, C. Klewe, J.-M. Schmalhorst, F. Bertram, O. Kuschel, T. Schemme, J. Wollschläger, S. Francoual, J. Stempfer, A. Gupta, M. Meinert, G. Götz, D. Meier, and G. Reiss, *Phys. Rev. Lett.* **115**, 097401 (2015).
- [34] C. Klewe, T. Kuschel, J.-M. Schmalhorst, F. Bertram, O. Kuschel, J. Wollschläger, J. Stempfer, M. Meinert, and G. Reiss, *Phys. Rev. B* **93**, 214440 (2016).
- [35] J. Krieff, D. Graulich, A. Moskaltsova, L. Bouchenoire, S. Francoual, and T. Kuschel, *J. Phys. D* **53**, 375004 (2020).
- [36] P. Weiss and R. Forrer, *Ann. Phys.* **10**, 279 (1929).
- [37] S. Celotto, W. Eerenstein, and T. Hibma, *Eur. Phys. J. B* **36**, 271 (2003).
- [38] A. V. Ramos, J.-B. Moussy, M.-J. Guittet, A. M. Bataille, M. Gautier-Soyer, M. Viret, C. Gatel, P. Bayle-Guillemaud, and E. Snoeck, *J. Appl. Phys.* **100**, 103902 (2006).
- [39] J.-B. Moussy, S. Gota, A. Bataille, M.-J. Guittet, M. Gautier-Soyer, F. Delille, B. Dieny, F. Ott, T. D. Doan, P. Warin, P. Bayle-Guillemaud, C. Gatel, and E. Snoeck, *Phys. Rev. B* **70**, 174448 (2004).